$NaAlH_4$ nanoconfinement in a mesoporous carbon for application in lithium ion batteries

L. Silvestri[a,b,z], A. Paolone[c], L. Cirrincione[d], P. Stallworth[d], S. Greenbaum[d,*], S. Panero[a,*], S. Brutti[c,e*] and P. Reale[b]

a. Dipartimento di Chimica, Sapienza Università di Roma, P. le Aldo Moro 5, Roma (Italy);

b. ENEA Centro Ricerche Casaccia, via Anguillarese 301, Roma (Italy);

c. Istituto dei Sistemi Complessi (ISC-CNR), P.le Aldo Moro 5, Roma (Italy);

d. Department of Physics and Astronomy, Hunter College of the City University of New York, NY 10065, New York (USA);

e. Dipartimento di Scienze, Università della Basilicata, V.le dell'Ateneo Lucano 10, Potenza (Italy).

z. l.silvestri@uniroma1.it

Abstract

Alanates have recently attracted attention as new anodic materials for lithium ion batteries. The electrochemical activity of sodium alanate has been previously reported and its conversion mechanism explained. Through a complex conversion reaction, this compound is able to use virtually all of its theoretical capacity, achieving more than 1700 mAh/g upon its first discharge with an efficiency of 70%. Nevertheless the alanate exhibits capacity fading within a few cycles. This is mainly due to the severe structural reorganization following the conversion reaction, which can result in electrode pulverization and loss of electrical contact. Here, we present a nanocomposite material, consisting of $NaAlH_4$ confined within a nanoporous carbon matrix, that is capable of improving cyclability by mitigating the effects of volume expansion. Specifically, the nanocomposite has been studied in terms of structure, morphology and hydrogen content by the means of infrared spectroscopy, solid state nuclear magnetic resonance, electronic microscopy and thermal analysis. Finally, the performance of the nanoconfined alanate in lithium cells is presented.

Introduction

Anodic materials based on conversion chemistries could represent a viable alternative to the classical intercalation materials currently used in lithium ion devices[1-3]. According to the general scheme $M_xX_y + ne^- + nLi^+ \leftrightarrow xM^0 + yLi_mX$ ($m = n/y$), this class of materials is theoretically capable of exchanging up to two or more electrons per redox center. This implies a considerable capacity enhancement, and if exploited, could exceed the capacity limits intrinsic to typical intercalation/de-intercalation processes.

Included in this group of materials are metal hydrides such as MgH_2, whose electrochemical potential was identified and characterized by Tarascon et al. in 2008 [4]. Hitherto, few related studies have been reported and most of these primarily concern binary metal hydrides[5-8]. On the other hand, other hydride systems have been tested in lithium cells, where performance studies for materials based upon alanates have been especially promising[9-11]. In particular, sodium alanate was proven to be a feasible candidate for electrochemical applications[12]. These reports have shown that upon discharge $NaAlH_4$ [10,11] very nearly achieves its theoretical capacity (1985 mAh/g), although it has a poor recharge efficiency due to the severe structural reorganization in the conversion reaction[13,14]. In battery tests this causes electrode pulverization leading to critical damage to the mechanical integrity of the cell and loss of electrical contact[15].

Mechanochemical treatments appear to provide an effective solution towards improving the electrochemical performance of sodium alanate in lithium cells. When employed, these techniques demonstrate an increased coulombic efficiency in the whole discharge-recharge cycle from 30% to 70% [10,11], otherwise capacity fade occurs within a few cycles. One method that has been shown to highly enhance the cycle life stability[16,17] is that of dispersing the active material in a nanoporous carbon matrix. Besides preserving conductivity, the presence of carbon is beneficial towards preventing grain growth and sintering by limiting the large volumetric changes encountered during lithium incorporation/de-incorporation[18]. Along these lines, in order to improve the performance of sodium alanate in electrochemical cells, a nanocomposite of sodium alanate confined in a mesoporous carbon host matrix has been developed. A solvent-assisted infiltration method was chosen to highly disperse $NaAlH_4$ as well as facilitate a close contact with the carbon material[19]. The success of the infiltration method can be gauged by morphological and thermal analysis. The interaction between the carbon matrix and the sodium alanate was studied by infrared spectroscopy and solid state nuclear magnetic resonance (NMR). Finally, electrochemical characterization is carried out by galvanostatic measurement.

Experimental

Materials - $NaAlH_4$ (hydrogen grade), resorcinol (≥ 99 %), formaldehyde (37 wt.% in H_2O) and anhydrous tetrahydrofuran (≥ 99.9 %) were purchased from Sigma Aldrich and used without any pretreatment. Anhydrous sodium carbonate was purchased from Carlo Erba Reagents.

Sample preparation - The carbon aerogel was synthesized by polycondensation of resorcinol with formaldehyde according to a method developed by Pekala et al.[20], followed by solvent exchange and pyrolysis. In particular, 4 g of resorcinol ($C_6H_4(OH)_2$) were dissolved in 5.88 g of distilled water with 7.62 mg of sodium carbonate (Na_2CO_3) as the basic catalyst. 5.83 g of formaldehyde (CH_2O) were added and the resulting solution was stirred for 1 hour at room temperature. Then, the solution was aged 12 hours at 90° C. Following this, the batch was cooled to room temperature, washed with acetone three times to remove the excess water and catalyst and allowed to dry in air. The resulting formaldehyde-resorcinol aerogel sample was pyrolized in a tube furnace under an argon atmosphere at 750° C for 4 hours, yielding a carbon aerogel (CRF). Before using, the carbon aerogel was further subjected to a 500° C thermal treatment under vacuum for 20 hours, in order to remove any adsorbed species. The product was then moved to an argon filled glove box.

In order to prepare the $NaAlH_4$/carbon nanocomposite, a quantity of sodium alanate was measured in order to fill 50% of the total porous volume of the carbon host. This corresponded to a carbon/$NaAlH_4$ weight ratio equal to 0.624/0.376. Infiltration was carried out as follows: the $NaAlH_4$ and carbon aerogel powders were mixed in a mortar, anhydrous tetrahydrofuran (THF) was added dropwise to promote the alanate dissolution and precipitation into the carbon pores. The mixture was then dried under vacuum for 5 hours in order to drive-off the solvent and allow for the recrystallization of $NaAlH_4$. A few samples of this $NaAlH_4$/carbon nanocomposite were identically prepared, and in this report are all referred to as *si*. Also, a control sample was prepared by mixing the same dry quantities of $NaAlH_4$ and carbon aerogel using a mortar and pestle. This control sample was labeled as *ni*. Table 1 summarizes the two sample preparation routes.

Characterization - Porous volume, pore size and surface area of the CRF were determined with N_2 adsorption at 77 K using a Quantachrome Instruments Autosorb IQ. Data obtained were analyzed using the Brunauer-Emmett-Teller (BET)[21] equation to calculate surface area, t-plot[22] for microporosity analysis and the Barrett-Joyner-Halenda (BJH)[23] method for mesoporosity analysis, as implemented in the Quantachrome ASiQWin software. The sample morphology was further investigated through high-resolution scanning electron microscopy using a LEO 130 HRSEM and transmission electron microscopy using a FEI Tecnaicryo-TEM instrument. FTIR spectra were

acquired using a Bruker Alpha spectrometer. All spectra were recorded in the wave number range between 2000 and 400 cm^{-1}, in transmission mode at room temperature. The FTIR samples were prepared from fine CRF powders mixed with KBr in a 1:100 weight ratio (powder to KBr respectively) and then hand pressed into pellets by a Pike die set. FTIR assignments were made by comparing with literature data[24].

Thermal analysis was carried out with a Perkin Elmer diamond TGA/DTA. For this characterization, the sample was first heated at 50 °C under argon flow (in order to eliminate residual THF from the *si* composite) until equilibration of the weight. After this, the temperature scan was performed to 450 °C at a rate of 5 °C/min under Ar flow.

For electrochemical tests, electrodes were prepared from a powder mix of *si* powder, SuperP and PVdF (polyvinylidene difluoride) as binder in weight ratio of 7:1:2. The powder was cold pressed onto 10 mm diameter Cu disks. Three electrode cells were assembled with the *si* based electrode as the working electrode and lithium metal foil as the counter electrode. LP30, (Merck; 1M $LiPF_6$ in 1:1 v/v ethylene carbonate–dimethyl carbonate) embedded in a Whatmann borosilicate fiber disk was used as the electrolyte. Electrochemical performance tests were carried out using a Maccor battery cycler under galvanostatic condition in a voltage range of 0.01-2.5 V and current density of 20 mA/g.

Magic angle spinning nuclear magnetic resonance (MAS) measurements were performed on a Varian Direct Drive 300 MHz spectrometer with a magnetic field of 7.1 T operating at Larmor frequencies of 79.4 MHz for ^{23}Na (spin 3/2) and 78.2 MHz for ^{27}Al (spin 5/2)**.** Samples are highly sensitive to ambient laboratory conditions, therefore in preparation for NMR study, samples were packed into 1.6 mm zirconia rotors inside a glove box within an Argon atmosphere. In order to maintain the integrity of the samples during measurement dry N_2 gas was used for both MAS and purge. MAS rates between 35 kHz and 40 kHz were used. Data were gathered using single pulse and rotosynchronized echo pulse sequences (*pulse* - τ - *pulse* - τ – *acquire*, 25 μs ≤ τ ≤ 30μs). High power short pulses (1μs) were employed in order to minimize artifacts and phase distortions in the lineshapes. Spectra are referenced to 1M NaCl aqueous solution for ^{23}Na and to 1M $AlCl_3$ aqueous solution for ^{27}Al.

Results and discussion

The as-synthesized carbon matrix obtained by aerogel pyrolysis before the alanate infiltration was characterized in terms of its residual oxygen content and morphology. Elemental analysis demonstrated an oxygen content of 1.75 wt.%. This oxygen level is not reduced by

performing the aerogel pyrolysis under a flow of reducing Ar/H_2 gas at 750 °C for 8 hours (data not shown), as it is likely related to the expected presence of native C=O groups on the graphitic-like nano-domains (see below).

N_2 physisorption was employed to analyze the porosity of the carbon aerogel, and the corresponding experimental adsorption-desorption isotherms are shown in figure 1. The curve rises almost vertically at low relative pressure, followed by an inflection point. After that, through a smaller slope, the adsorbed volume continues to rise throughout the intermediate zone. Finally at high relative pressure, the slope increases again. The major feature of this isotherm is the presence of hysteresis between the adsorption/desorption branches. The hysteresis loop is associated with the filling and emptying of mesopores by capillary condensation. According to the IUPAC classification, the obtained isotherm is a mixed II/IV type, typical of meso-macroporous materials. The overall surface area, calculated by the BET equation, is 672 m^2/g with a total porous volume of 1.33 cm^3/g and $V_{meso}/V_{microporosity}$ ratio of 1.13/0.2. The average pore width is 16 nm calculated by the BJH method from the desorption branch of the isotherm.

The sample morphologies before and after infiltration have been analyzed by both scanning electronic microscopy (SEM) and transmission electronic microscopy (TEM). Figure 2 shows the micrographs of the *ni* and *si* samples, along with pristine $NaAlH_4$ and CRF as reference materials. The CRF sample shows a large porosity (figure 2a-b), as it consists of an open structure constituted by spherical particles interconnected with open pores on the surface. On the other hand, the pristine alanate (figure 2c-d) has regular plate-like particles with variable dimensions in the range of 1μm - 100 nm. After mixing with CRF (*ni* sample, figure 2e-f), the $NaAlH_4$ particles assume rod-like shapes. SEM images distinguish the two components of the mixture, i.e. alanate and carbon matrix, however, a certain interaction upon mixing occurs, since the $NaAlH_4$ morphology is markedly altered. After infiltration, the SEM image (*si* sample, figure 2g-h) reveals a homogeneous composite material: the alanate is deeply permeated into carbon support without evident phase separation. Moreover, the superficial porosity of the host carbon appears to have decreased. Efforts were made to analyze the phase nature via XRD measurements (data not shown). The diffraction data revealed a pure $NaAlH_4$ phase for the *ni* sample; however, no definitive patterns were evident for the *si* sample, and it was concluded that the infiltrated phases were highly disordered.

Aspects of the sample local structures are revealed in the collection of FTIR spectra given in figure 3. CRF exhibits residual oxygenated functional groups along its surfaces, as mentioned previously, due to incomplete carbonization of the sample during the pyrolysis. The typical asymmetric stretching mode of C=O groups is observed at 1590 cm^{-1}. The broad peak at 1110 cm^{-1} along with a shoulder at 1240 cm^{-1} corresponds to C-O stretching modes of methylene ether bridge

and phenolic groups respectively. The *ni* sample exhibits typical vibrational modes of $NaAlH_4$. Signals related to the carbon matrix are not evident due to their lower relative intensity. The peaks at 1675 and 1430 cm^{-1} and peaks at 904 and 743 cm^{-1} are assigned to Al-H stretching and H-Al-H bending modes of the $[AlH_4]^-$ group respectively. Despite oxygenated functional groups in the carbon aerogel, the matrix remains relatively inert as there is apparently no reaction with sodium alanate upon simple grinding, as seen for the *ni* sample. It is of interest to look for the characteristic vibrational frequencies exhibited by $NaAlH_4$ after infiltration. The Al-H stretching mode at 1675 cm^{-1}, which is very broad and intense for the pristine and *ni* samples, is weak for the *si* sample. The stretching band related to C=O groups near 1590 cm^{-1} in the *si* sample is probably due to the formation of aluminum carboxylates. The broad band around 1426 cm^{-1} for the *si* (absent in the *ni*) sample is associated with the stretching modes of Al-H in Na_3AlH_6. The *si* sample also exhibits broad superimposed bands within the bending region of $NaAlH_4$. For instance, the $\delta[AlH_4]^-$ mode of $NaAlH_4$ at 904 cm^{-1} is shifted to 877 cm^{-1}, and the shoulder around 840 cm^{-1} appears to be aligned with the $\delta[AlH_6]^{3-}$ mode of Na_3AlH_6. The H-Al-H bending mode at 713 cm^{-1} of $NaAlH_4$ appears to be split for *si* and *ni* into peaks at 743 and 693 cm^{-1}.

Further insights can be obtained from solid state ^{23}Na and ^{27}Al MAS NMR measurements. A few alanate infiltrated samples were prepared and since a fair degree of NMR spectral intensity variation was observed, it is concluded that some heterogeneity exists between these identically prepared materials. The infiltration of $NaAlH_4$ into the carbon matrix strongly affects the NMR spectra in the differences of constituent peak positions and isotropic distributions. Figure 4 compares NMR spectra for *si*, *ni* and reference materials ($NaAlH_4$ and Na_3AlH_6). The spectra are interpreted in terms of contribution resonances from constituent phases. The ^{23}Na spectrum for the *ni* sample is entirely due to $NaAlH_4$ with no resonances associated with metallic Na or Na_3AlH_6. The ^{27}Al spectrum for *ni* shows the large alanate component as well as a small oxide peak. These observations are consistent with the simple alanate-carbon mix fabrication description for *ni*, although there appears to be some slight reaction product likely between the alanate and surface oxygenated carbon species.

An altogether different picture emerges for the *si* sample. In this case, due to the decrease in particle size and structural distributions as a result of infiltration, there are correspondingly large distributions in the quadrupolar coupling constants for both ^{23}Na and ^{27}Al spectra. As a consequence, spinning sidebands are broad with greatly reduced intensity (as compared to the *ni* spectra). The lineshape variations between the different *si* samples, indicate the overall ^{23}Na signal is a composite of a number of overlapping resonances from distinct Na sites. Isotropic peaks are evident at -9 ppm and +4 ppm (no metallic ^{23}Na resonances are observed), and there is a broad

unresolved feature underneath the peaks. Freitas et al.[25] measured the ^{23}Na resonance within the range of 0 to -30 ppm for Na^+ infused carbon (with a much smaller average pore size than that reported here). This Na site was characterized by a large quadrupole coupling constant of about 1.2 to 1.8 MHz. Their results are interpreted along the lines of Na^+ bound to oxygenated carbon groups (i.e. carbonyl) at pore surfaces. A similar description may account for the broad feature encountered here. Contrary to the FTIR findings, there are no resolved features that can be assigned to Na_3AlH_6. The small resonance at -9 ppm reveals a portion of the initial $NaAlH_4$ that survived infiltration. The dominant ^{23}Na peak centered near +4 ppm is due to Na sites influenced by substantial interaction with electron withdrawing oxygen species such as carbonates[26] and peroxides[27].

Unfortunately the -9 ppm signal is not easily quantified here since the unresolved sideband structure is an unkown mixture of 1st-order quadrupolar satellite intensity from the various Na sites. In principle it is possible to obtain an estimate of the alanate content from the ^{27}Al NMR, but these MAS results show no evidence of a signature peak near +96 ppm. Instead, the ^{27}Al spectrum shows three resonances near +70, +35 and +4 ppm. There is also a large metallic Al signal at +1640 ppm (not shown), the intensity of which varies roughly between 20% and 50% of the overall detected signal with the sample heterogeneity. Some likely assignments include 4-coordinated Al-oxides (from about +50 to +85 ppm)[28] and 6-coordinated Al-oxides (from -20 to +35 ppm)[29], and Al-carboxylates (~ 0 ppm)[30,31]. It is noted that both ^{23}Na and ^{27}Al signatures for *si* somehow resemble spectra of an amorphous (unannealed) phase of $NaAl_9O_{14}$ by MacKenzie et al.[32], although those ^{23}Na and ^{27}Al resonances display large 2nd-order quadrupolar interactions, have somewhat more shielded shifts and probably display intense sideband manifolds. In addition to the site distribution, some broadening and shifts observed for *si* might be attributed to the susceptibility of the carbon matrix[28]. This effect has been observed, but only accounts for a shielding of roughly -2 ppm; not nearly enough to draw attention to the +70 ppm peak. However, large distributions are present and the presumed some ^{27}Al signal intensity attributable to $NaAlH_4$ is likely within this unresolved portion.

Both FTIR and NMR spectroscopies show that strong chemical interactions occur between $NaAlH_4$ and the carbon support upon infiltration. Some $NaAlH_4$ survives infiltration intact, although the absolute content is not readily available from the data. All signals observed for *si*, e.g. the ^{23}Na NMR, ^{27}Al NMR and Al-H stretching mode, are broadened (in the case of NMR by discrete isotropic distributions) and are largely different from either $NaAlH_4$ or Na_3AlH_6 references. For the most part compared to $NaAlH_4$, these resonances for *si* reflect Na and Al environments that are greatly altered due to nanoconfinement.

From another perspective, the net amount of active material after infiltration has been evaluated by thermogravimetric analysis (TGA). Figure 5 shows the thermal desorption profiles of pristine $NaAlH_4$, *ni* and *si* samples. The bulk $NaAlH_4$ sample releases approximately 7.2 wt.% H_2 at the end of the temperature scan through the expected multistep mechanism[33].

$$NaAlH_4 \leftrightarrow 1/3Na_3AlH_6 + 2/3Al + H_2$$
$$Na_3AlH_6 \leftrightarrow NaH + Al + 3/2H_2$$
$$NaH \leftrightarrow Na + 1/2H_2.$$

The amount of H_2 released nearly reaches the theoretical value of 7.4 wt% H_2 with respect of $NaAlH_4$, with the discrepancy attributed to the presence of trace impurities in the starting material. When mixed with CRF, the hydrogen release follows a different thermal desorption profile. Note that the *ni* sample starts to decompose about 190 °C and proceeds through a massive single step. At the end of the temperature scan it reveals a 6.6 wt.% loss. In the case of the *si* sample, mass loss starts above 60-80 °C and continues throughout in a single smooth process. After the temperature scan (up to 450 °C) approximately 4 wt.% of hydrogen is released from the infiltrated sample with respect to the $NaAlH_4$ mass. This is much less than the 6.6 wt.% loss of the *ni* sample, and must be related to the oxidization processes upon infiltration, e.g. beyond that expected of the intrinsic oxygen present in the carbon matrix (1.75 wt.%). Furthermore, considering the extraordinary conditions realized by infiltration/nanoconfinement (a saturated alanate solution finely dispersed throughout a highly porous carbon matrix), it is well known that some hydrogen desorption is possible via the catalytic ability of the nanocarbon[34-36]. Additional reactions with THF and possible impurities upon infiltration cannot be excluded. Nevertheless part of the infiltrated material remains functional with 54% of the hydrogen content still available for thermal desorption and possibly for electrochemical conversion.

Electrochemical performance tests of synthesized $NaAlH_4$/CRF nanocomposites have been carried out under galvanostatic conditions in lithium cells. Figure 6a shows the potential profiles of *ni* and *si* samples in comparison with pristine $NaAlH_4$ during the first discharge/recharge cycle. As described in previous work[10], pristine $NaAlH_4$ achieves almost 1700 mAh/g during the first discharge, where the profile is characterized by three sloped plateaus around 0.41, 0.26 and 0.17 V. Upon recharge only the 30 % of the exchanged capacity is returned. Nevertheless, oxidation proceeds in two steps around 0.40 and 0.47 V. When the alanate is mixed with the carbon aerogel the total capacity exchanged at the end of discharge is lower, reaching approximately 500 and 1000 mAh/g for *ni* and *si* samples, respectively. It is important to note that the experimental capacities shown in figure 6 are normalized by the total electrode mass including: the CRF carbon host, the

polymer binding and the conductive additive. Considering that the $NaAlH_4$:CRF weight ratio in the sample is about 0.37:0.64 and assuming a theoretical capacity of 1985 mAh/g for $NaAlH_4$ and 200 mAh/g for CRF [37], the capacity attributable to the $NaAlH_4$/CRF composite can be calculated as 862 mAh/g.

In the case of the non-infiltrated sample, *ni*, discharge evolves through three sloping plateaus centered at 0.4, 0.23 and 0.15 V. Upon recharge just 38% of developed capacity is returned and the voltage profile is characterized by three slopes at 0.4, 0.46 and 0.49 V. For the infiltrated sample (*si*) reduction occurs in a similar way through three slopes centered at 0.38, 0.25 and 0.11 V; however improved in that the coulombic efficiency rises to 55%, reaching 527 mAh/g at the end of first recharge through a single step developed around 0.44 V. As evident in figure 6b, the exchanged capacity abruptly decreases upon the second cycle, even if the recharge efficiency markedly improves. Actually, despite the fact that the amount of actual cycled capacity is only a small percentage of the theoretical value, the composite shows improved cycling as compared to the bulk alanate, which fails completely in few cycles[10].

Conclusions

A carbon aerogel (CRF) was synthesized as host for $NaAlH_4$ nanoparticles. The obtained mesoporous carbon consisted of interconnected spherical nanoparticles, and formed an overall nanoporous matrix. Characterization yielded a total porous volume of 1.33 cm^3/g and average pore diameter of 16 nm. In order to improve the dispersion of $NaAlH_4$ particles into the carbon matrix, a solvent assisted method was used. The resulting nanocomposite (alanate particles fully dispersed into the carbon matrix) exhibited a homogeneous morphology. Nevertheless, the nanocomposite was highly reactive, disordered and chemically heterogeneous. As a consequence, the material was difficult to manage as it easily oxidized upon exposure to air, and tended to desorb hydrogen below 100 °C. Elemental analysis performed on the CRF revealed 1.75 wt.% of residual oxygen, which apparently is enough to promote intensive chemical interactions between the CRF and $NaAlH_4$. The total amount of infiltrated $NaAlH_4$ preserved after confinement seemed to be significant by FTIR measurements. Although this could not be substantiated via solid state NMR, the content was demonstrated to be only 54% by thermal analysis. Nevertheless the nanocomposite demonstrated improved cyclability inside a lithium cell. It is understood that confinement is effective in reducing electrode pulverization following the huge volume variations to which the alanate is subjected to upon lithium conversion.

In summary, this promising method of confining a hydrogen rich material via infiltration into a carbon aerogel appears to be capable of improving the reversibility of conversion reactions

within lithium cells. However, in order to counter the extensive decomposition of the sample after preparation, further improvements could proceed by optimizing the solvent-assisted infiltration method. For instance, this may be approached by improving the solvent purity, increasing carbon porosity, and grinding under a reducing hydrogen atmosphere (by ball milling in closed anaerobic vessels), or perhaps by an alternative melt infiltration technique[34]. Enhancements of the reversible cycled capacity, which may be linked to improvements in the chemical quality of the precursors, is essential for this composite material to be considered for application in electrochemical devices.

Acknowledgements

This work is carried out in the framework of the Italian project (FIRB-Futuro in ricerca 2010) "*Hydrides as high capacity anodes for lithium ion batteries"* (RBFR10ZWMO), supported by Italian Minister for University and Research. The authors would like to thank Dr. Antonio Rinaldi from ENEA for SEM images.

References

1. P. G. Bruce, B. Scrosati, and J. M. Tarascon, *Angew. Chem. Int. Ed.*, **47**, 2930 (2008).

2. J. Cabana, L. Monconduit, D. Larcher, and M. R. Palacín, *Adv. Mater.*, **22**, E170 (2010).

3. P. Poizot, S. Laruelle, S. Grugeon, L. Dupont, and J. M. Tarascon, *Nature*, **407**, 496 (2000).

4. Y. Oumellal, A. Rougier, G. A. Nazri, J. M. Tarascon, and L. Aymard, *Nat. Mater.*, **7**, 916 (2008).

5. Y. Oumellal, A. Rougier, J. M. Tarascon, and L. Aymard, *J. Power Sources*, **192**, 698 (2009).

6. S. Brutti, G. Mulas, E. Piciollo, S. Panero, and P. Reale, *J. Mater. Chem.*, **22**, 14531, (2012).

7. Y. Oumellal, W. Zaïdi, J. P. Bonnet, F. Cuevas, M. Latroche, J. Zhang, J. L. Bobet, A. Rougier, and L. Aymard, *Int. J. Hydrog. Energy*, **37**, 7831 (2012).

8. F. M. Vitucci, A. Paolone, S. Brutti, D. Munaò, L. Silvestri, S. Panero, and P. Reale, *J. Alloys Compd.*, **645**, S46 (2015).

9. L. Silvestri, S. Forgia, L. Farina, D. Meggiolaro, S. Panero, A. La Barbera, S. Brutti, and P. Reale, *ChemElectroChem*, **2**, 877 (2015).

10. L. Silvestri, L. Farina, D. Meggiolaro, S. Panero, F. Padella, S. Brutti, and P. Reale, *J. Phys. Chem. C*, **119**, 28766 (2015).

11. L. Cirrincione, L. Silvestri, C. Mallia, P. E. Stallworth, S. Greenbaum, S. Brutti, S. Panero, and P. Reale, *J. Electrochem. Soc.*, **163**, A2628 (2016).

12. J. A. Teprovich, J. Zhang, H. Colón-Mercado, F. Cuevas, B. Peters, S. Greenway, R. Zidan, and M. Latroche, *J. Phys. Chem. C*, **119**, 4666 (2015).

13. W. J. Zhang, *J. Power Sources*, **196**, 13 (2011).

14. G. A. Nazri and G. Pistoia, *Lithium Batteries*. Boston, Springer US (2003).

15. J. M. Tarascon and M. Armand, *Nature*, **414**, 359 (2001).

16. F. Schüth, *Chem. Mater.*, **26**, 423 (2014).

17. M. Winter and J. O. Besenhard, *Electrochimica Acta*, **45**, 31 (1999).

18. A. F. Gross, C. C. Ahn, S. L. V. Atta, P. Liu, and J. J. Vajo, *Nanotechnology*, **20**, 204005 (2009).

19. M. Christian and K. F. Aguey-Zinsou, *Nanoscale*, **2**, 2587 (2010).

20. R. W. Pekala, *J. Mater. Sci.*, **24**, 3221 (1989).

21. S. Brunauer, P. H. Emmett, and E. Teller, *J. Am. Chem. Soc.*, **60**, 309 (1938).

22. B. C. Lippens and J. H. de Boer, *J. Catal.*, **4**, 319 (1965).

23. E. P. Barrett, L. G. Joyner, and P. P. Halenda, *J. Am. Chem. Soc.*, **73**, 373 (1951).

24. J. C. Bureau, Z. Amri, P. Claudy, and J. M. Létoffé, *Mater. Res. Bull.*, **24**, 23 (1989).

25. J.C.C. Freitasa, M. A. Schettino Jr., F.G. Emmerich, A. Wong, M. E. Smith, *Solid State Nuclear Magnetic Resonance,* **32**, 109 (2007).

26. J. M. Egan and K. T. Mueller, *J. Phys. Chem. B,* **104**, 9580 (2000).

27. T. R. Krawietz, D. K. Murray, and J. F. Haw, *J. Phys. Chem. A,* **102**, 8779 (1998).

28. M. H. W. Verkuijlen, J. Gao, P. Adelhelm, J. M. van Bentum, P. E. de Jongh and A. P. M. Kentgens, *J. Phys. Chem. C,* **114**, 4683 (2010).

29. J. W. Akitt, *Prog. Nucl. Magn. Reson. Spectrosc.*, **21**, 1 (1989).

30. E. Zygadlo-Monikowska, Z. Florjanczyk , E. Rogalska-Jonska, A. Werbanowska, A. Tomaszewska, N. Langwald, D. Golodnitsky , E. Peled, R. Kovarsky, S.H. Chung, S. G. Greenbaum, *Journal of Power Sources,* **173**, 734 (2007).

31. R. Narayanan and R. M. Laine, *J. Mater. Chem.,* **10**, 2097(2000).

32. K. J. D. MacKenzie, M. E. Smith, M. Schmucker, H. Schneider, P. Angerer, Z. Gan, T. Anupold, A. Reinhold and A. Samoson, *Phys. Chem. Chem. Phys.*, **3**, 2137 (2001).

33. J. A. Dilts and E. C. Ashby, *Inorg. Chem.*, **11**, 1230 (1972).

34. T. K. Nielsen, M. Polanski, D. Zasada, P. Javadian, F. Besenbacher, J. Bystrzycki, J. Skibsted, and T. R. Jensen, *ACS Nano*, **5**, 4056 (2011).

35. C. Cento, P. Gislon, M. Bilgili, A. Masci, Q. Zheng, and P. P. Prosini, *J. Alloys Compd.*, **437**, 360 (2007).

36. A. Zaluska, L. Zaluski, and J. O. Ström-Olsen, *J. Alloys Compd.*, **298**, 125 (2000).

37. N. Liu, J. Shen, D. Liu, *Electrochimica Acta,* **97**, 271 (2013).

400

Table 1. List of the samples under investigation

Sample	**CRF:$NaAlH_4$ molar weight**	**Preparation**
ni	0.624:0.376	Physical mixing
si	0.624:0.376	Solvent assisted impregnation

401

Figure Captions

Figure 1. N_2 physisorption isotherm at 77K of CRF. Solid squares indicate adsorption branch, and empty squares indicate desorption.

Figure 2. Morphological analysis of a-b) CRF, c-d) $NaAlH_4$, e-f) *ni* and g-h) *si*. The top row a), c), e), and g) are SEM images, and the bottom row b), d), f), and h) are TEM micrographs.

Figure 3. FTIR spectra acquired in transmission mode of $NaAlH_4$/carbon before (*ni*) and after infiltration (*si*). For comparison, the reference FTIR spectra are from CRF, $NaAlH_4$ and Na_3AlH_6.

Figure 4. ^{23}Na (top) and ^{27}Al (bottom) MAS NMR spectra for infiltrated $NaAlH_4$/carbon and reference compounds $NaAlH_4$ and Na_3AlH_6.

Figure 5. Thermogravimetric analysis of pristine $NaAlH_4$, *ni* sample and *si* sample heated at 450 °C in Ar flow at 5 °C/min.

Figure 6. a) Voltage-Specific Capacity profile of the first discharge/recharge and b) Specific capacity versus cycle number before (*ni*) and after infiltration (*si*). $NaAlH_4$ was used as reference.

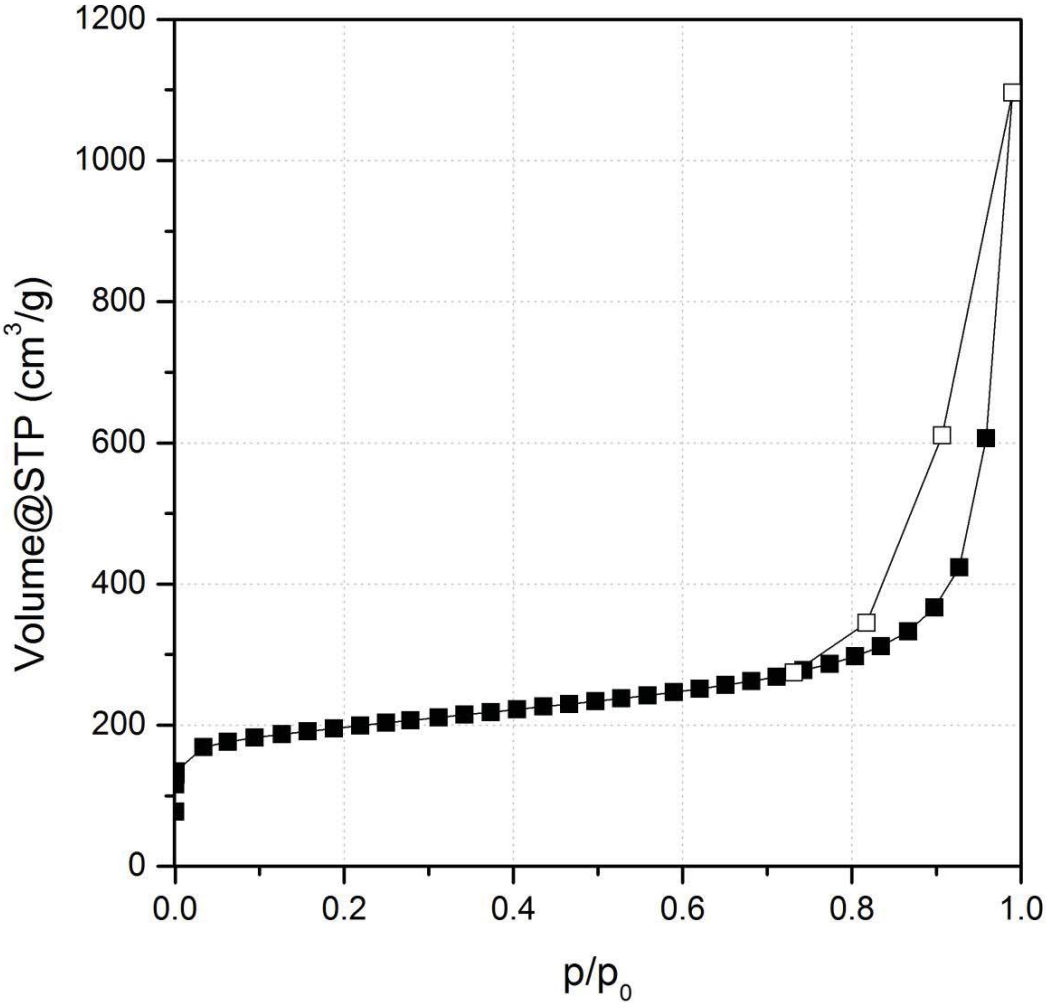
1200
1000
800
600
400
200
0
Volume@STP (cm3/g)
0.0
0.2
0.4
0.6
0.8
1.0
p/p0

a

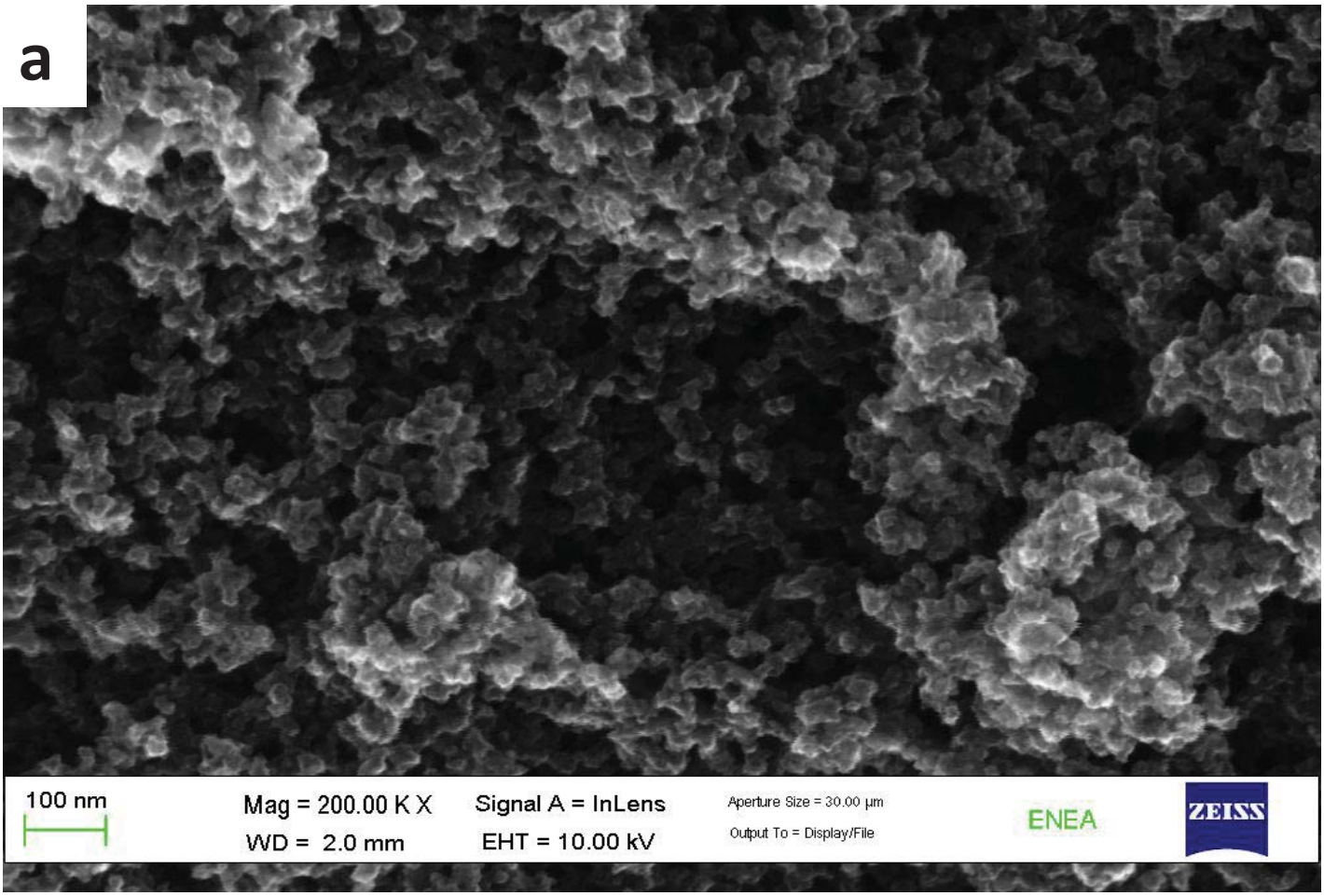
100 nm
Mag = 200.00 K X
WD = 2.0 mm
Signal A = InLens
EHT = 10.00 kV
Aperture Size = 30.00 µm
Output To = Display/File
ENEA
ZEISS

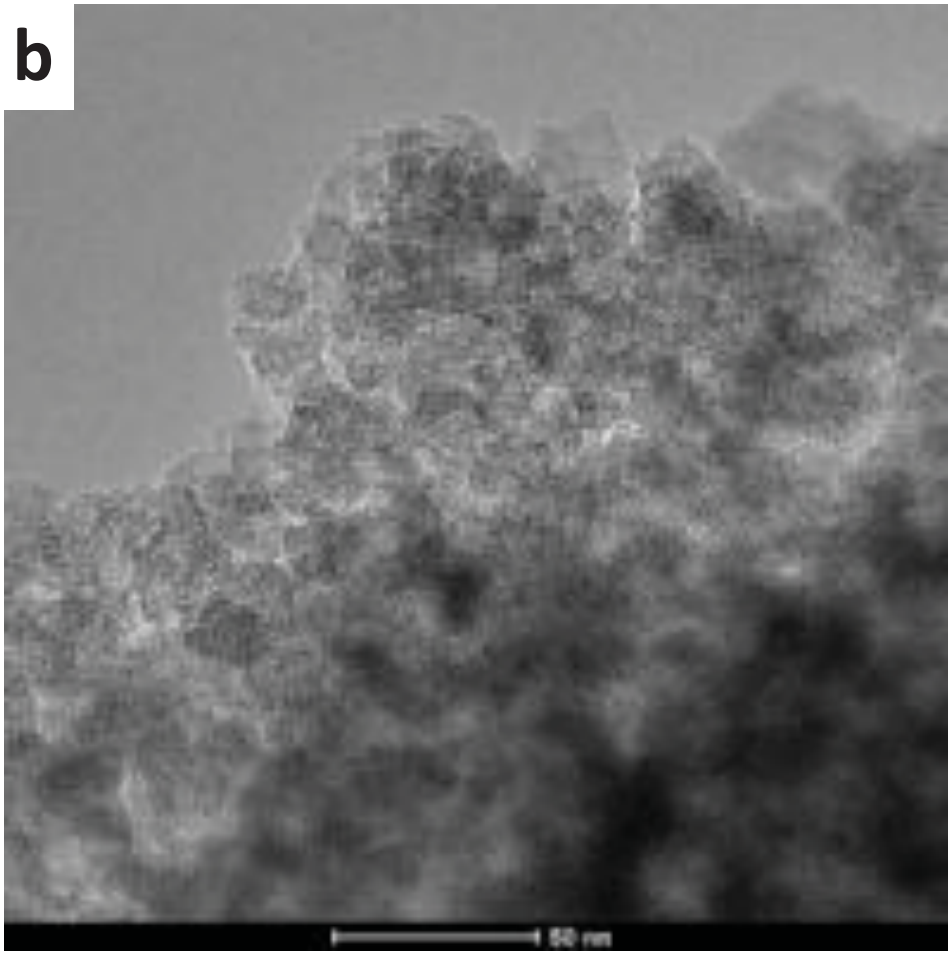
b
50 nm

C

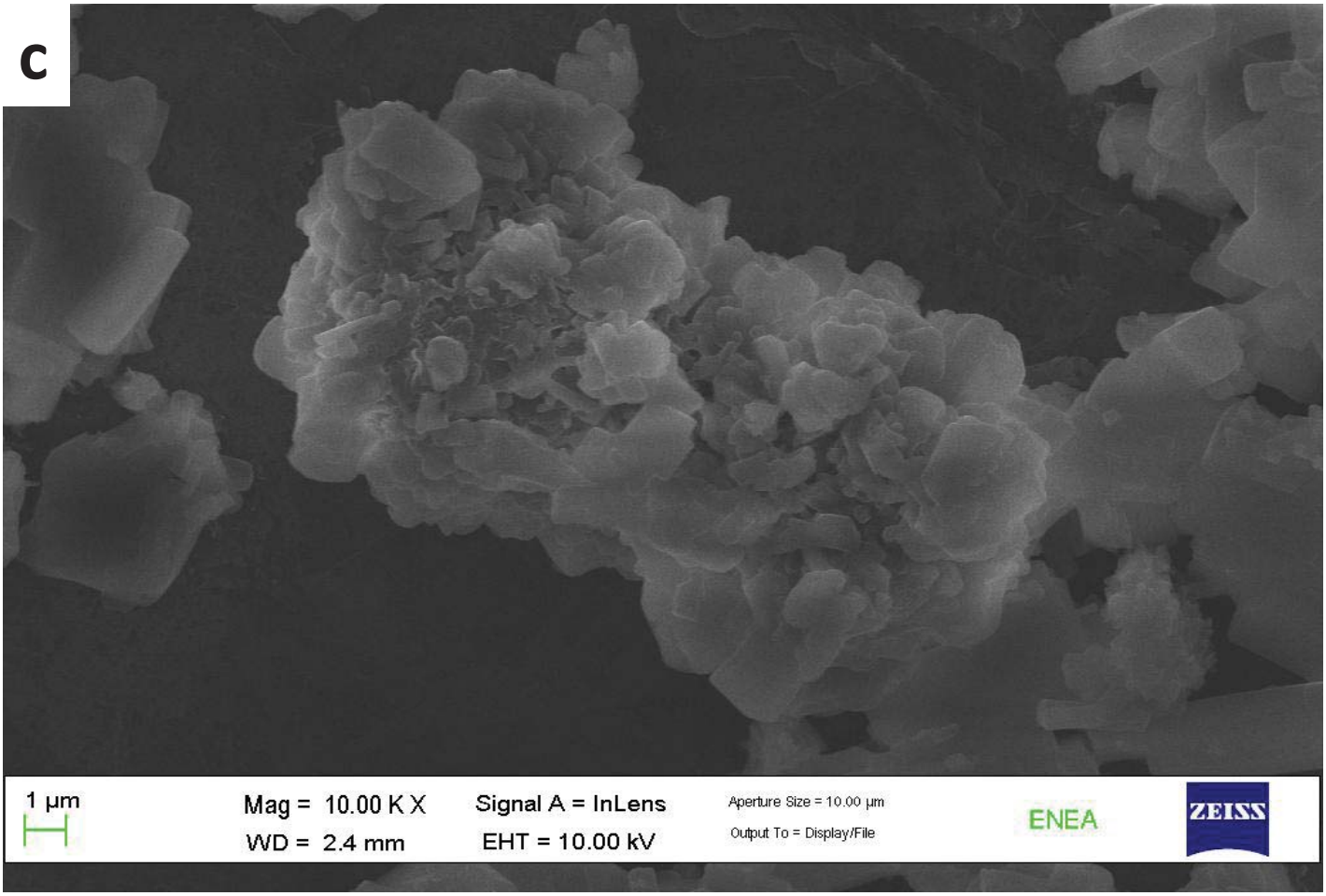
1 µm
Mag = 10.00 K X
WD = 2.4 mm
Signal A = InLens
EHT = 10.00 kV
Aperture Size = 10.00 µm
Output To = Display/File
ENEA
ZEISS

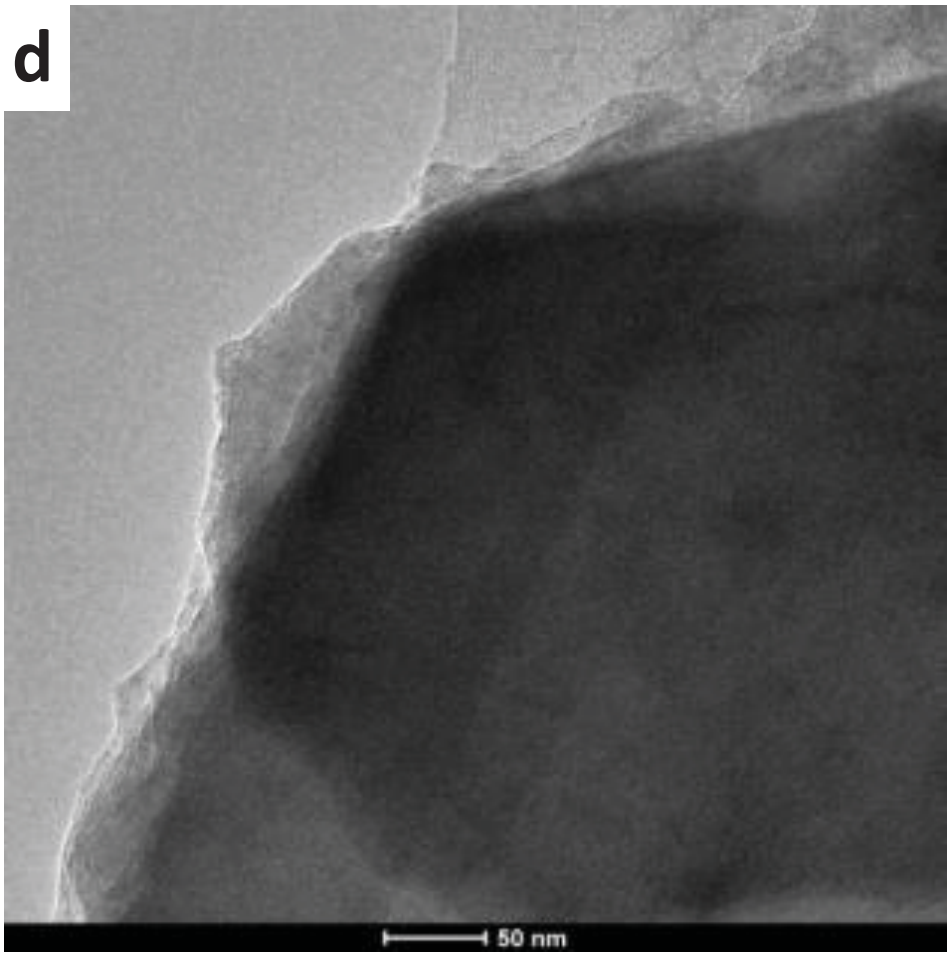
d
50 nm

e


1 µm
Mag = 10.00 K X
WD = 2.4 mm
Signal A = InLens
EHT = 10.00 kV
Aperture Size = 10.00 µm
Output To = Display/File
ENEA
ZEISS

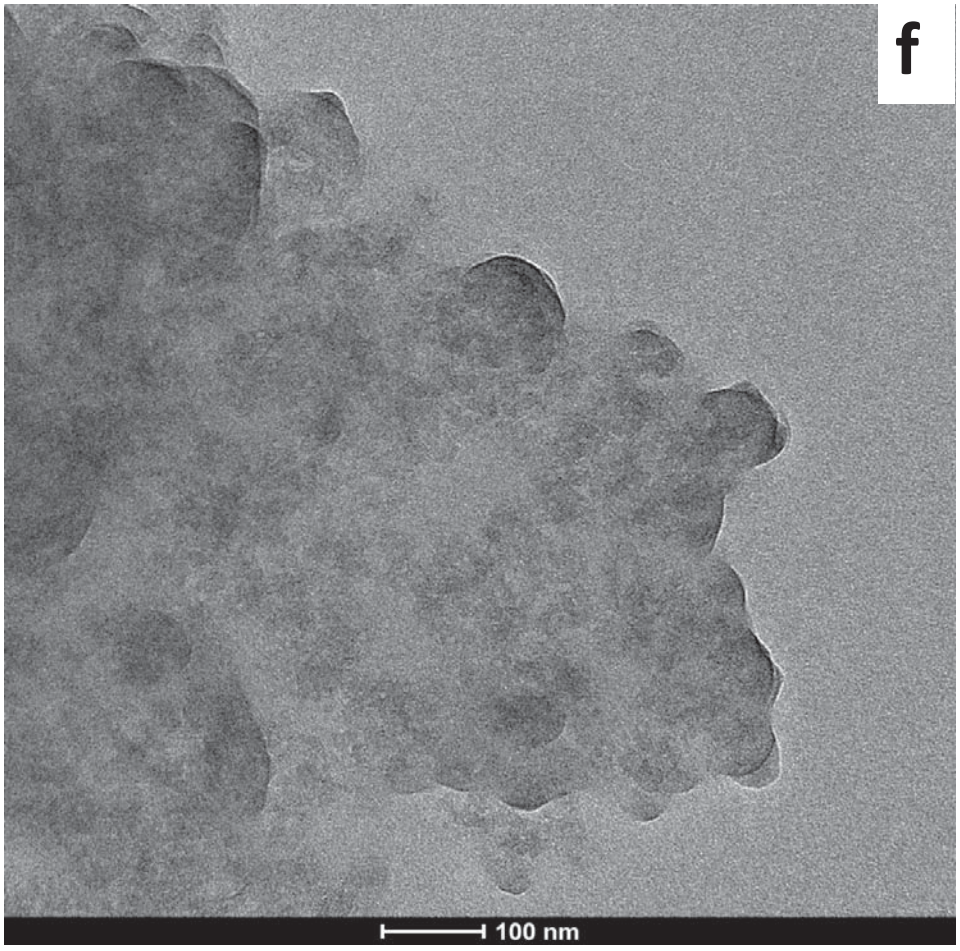
f
100 nm

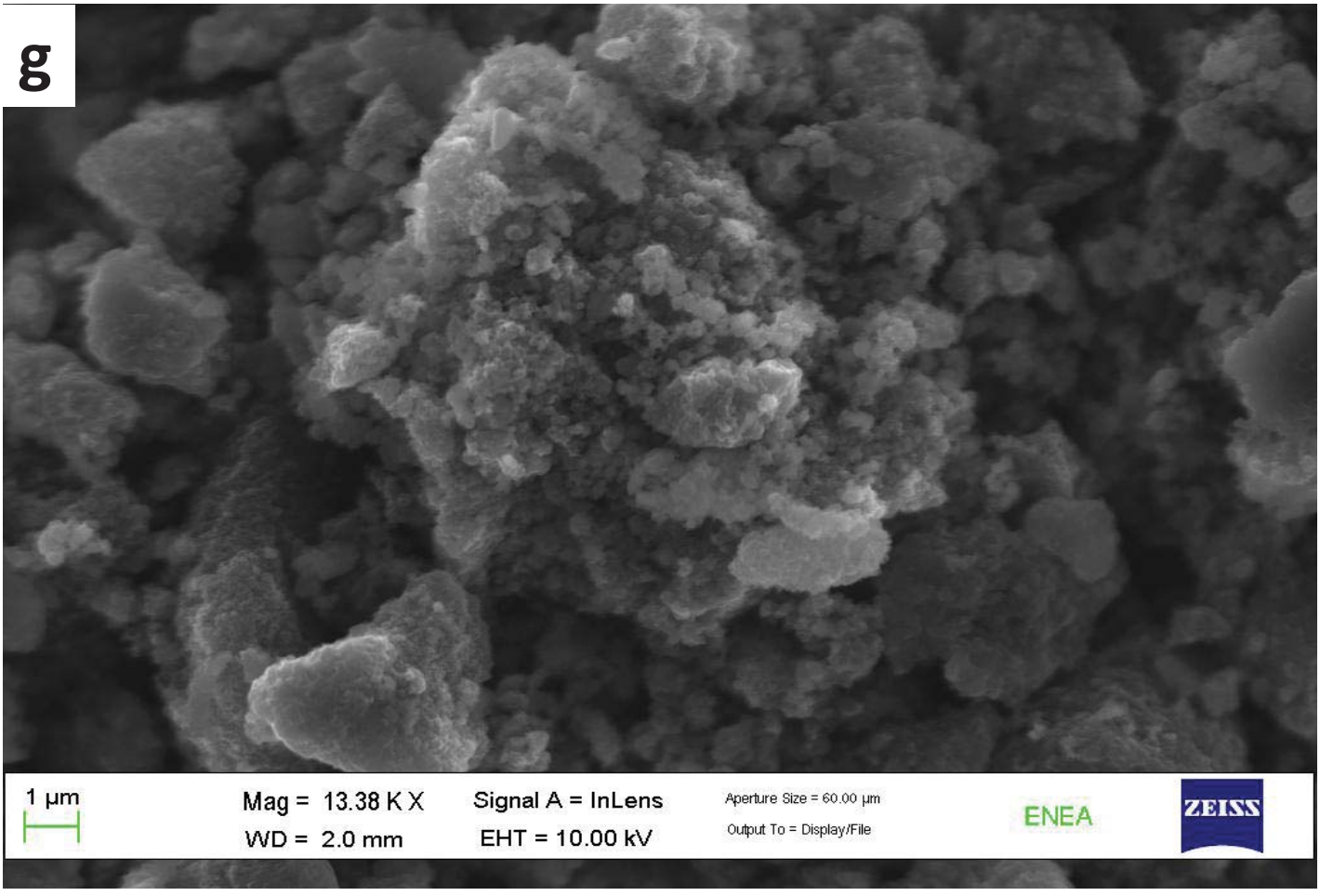
g
1 µm
Mag = 13.38 K X
WD = 2.0 mm
Signal A = InLens
EHT = 10.00 kV
Aperture Size = 60.00 µm
Output To = Display/File
ENEA
ZEISS

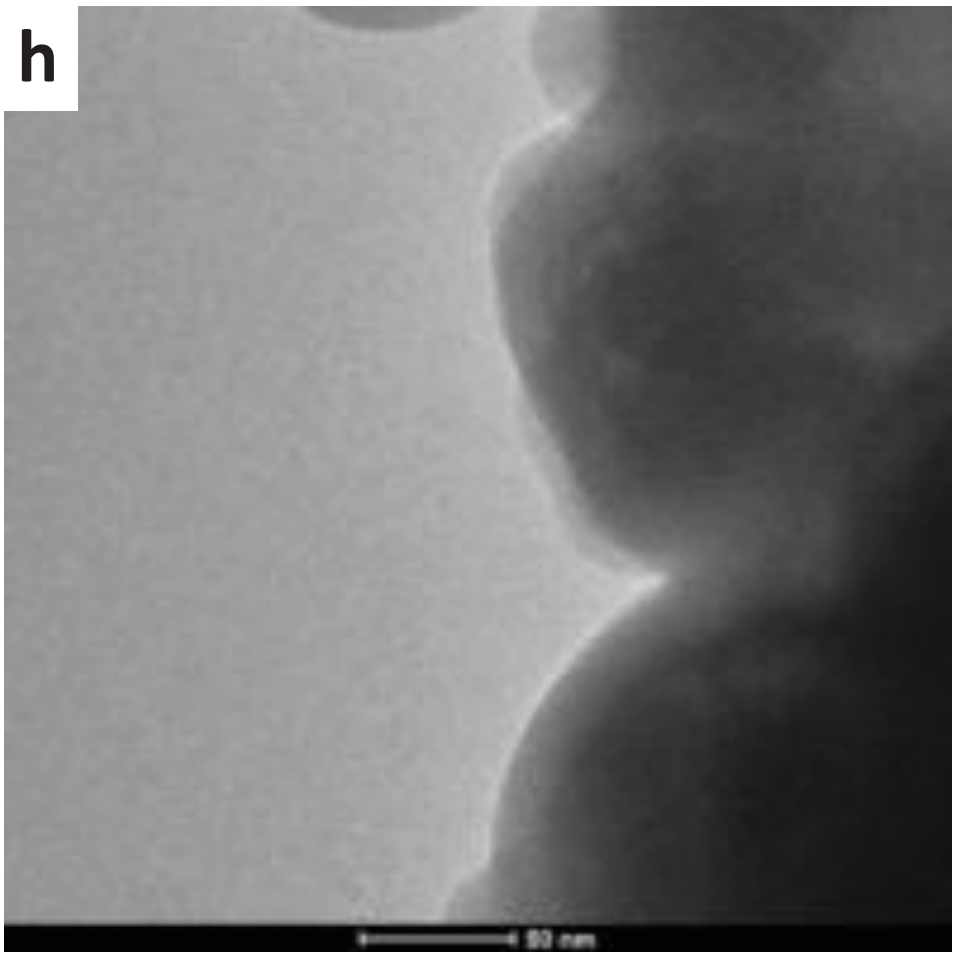
h
50 nm

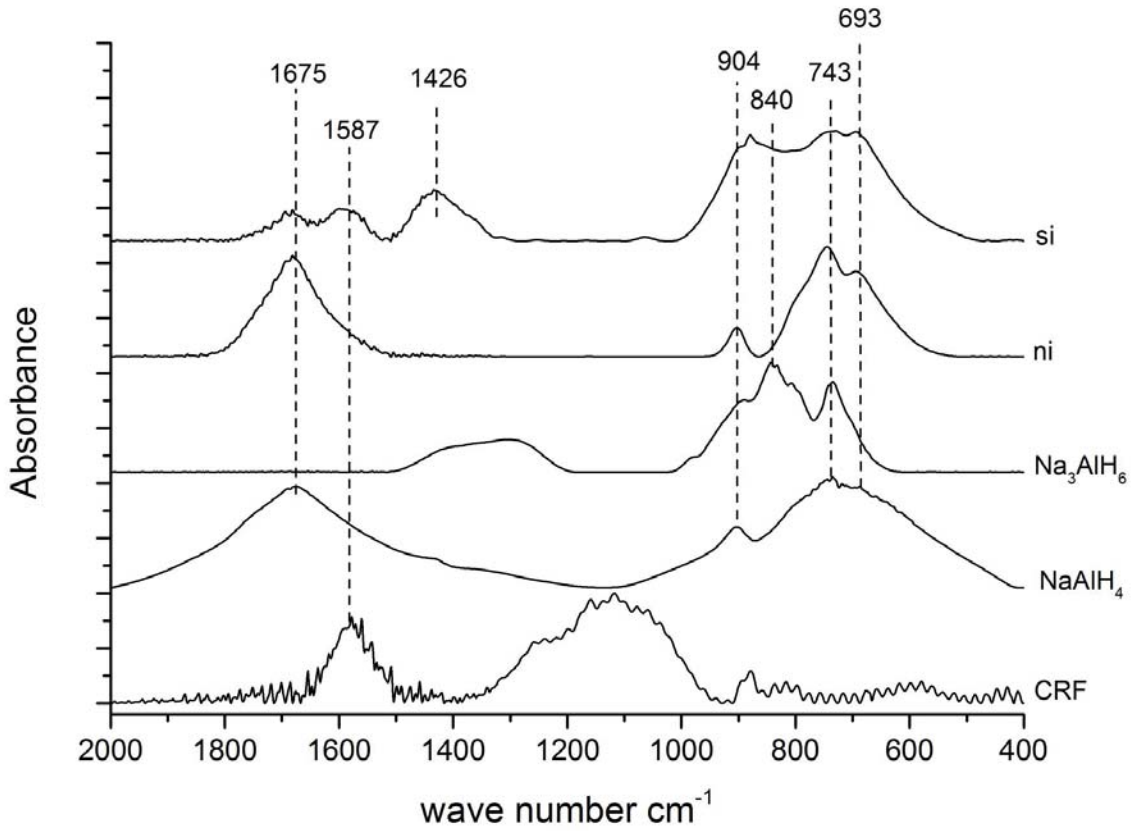
693
1675
904
1426
743
840
1587
si
ni
Na_3AlH_6
$NaAlH_4$
CRF
Absorbance
2000
1800
1600
1400
1200
1000
800
600
400
wave number cm^{-1}

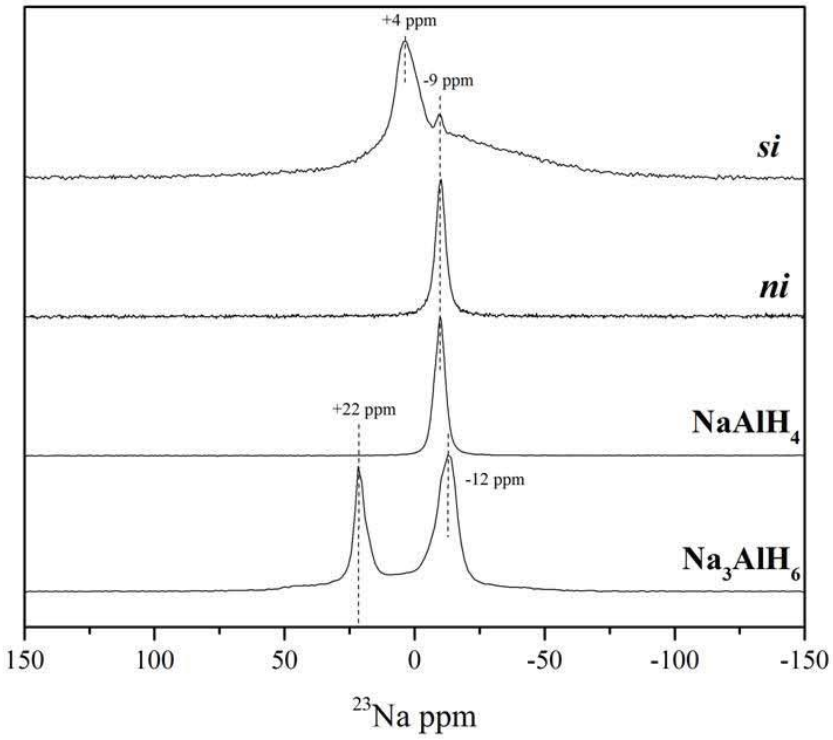
+4 ppm
-9 ppm
si
ni
+22 ppm
NaAlH4
-12 ppm
Na3AlH6
150
100
50
0
-50
-100
-150
23Na ppm

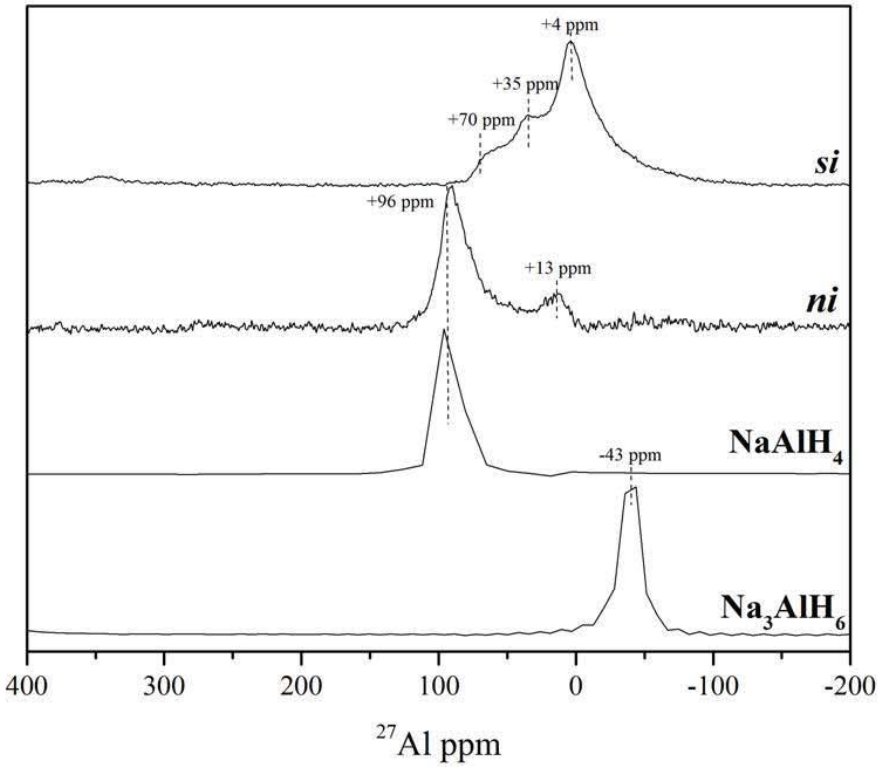
+4 ppm
+35 ppm
+70 ppm
si
+96 ppm
+13 ppm
ni
NaAlH4
-43 ppm
Na3AlH6
400
300
200
100
0
-100
-200
27Al ppm

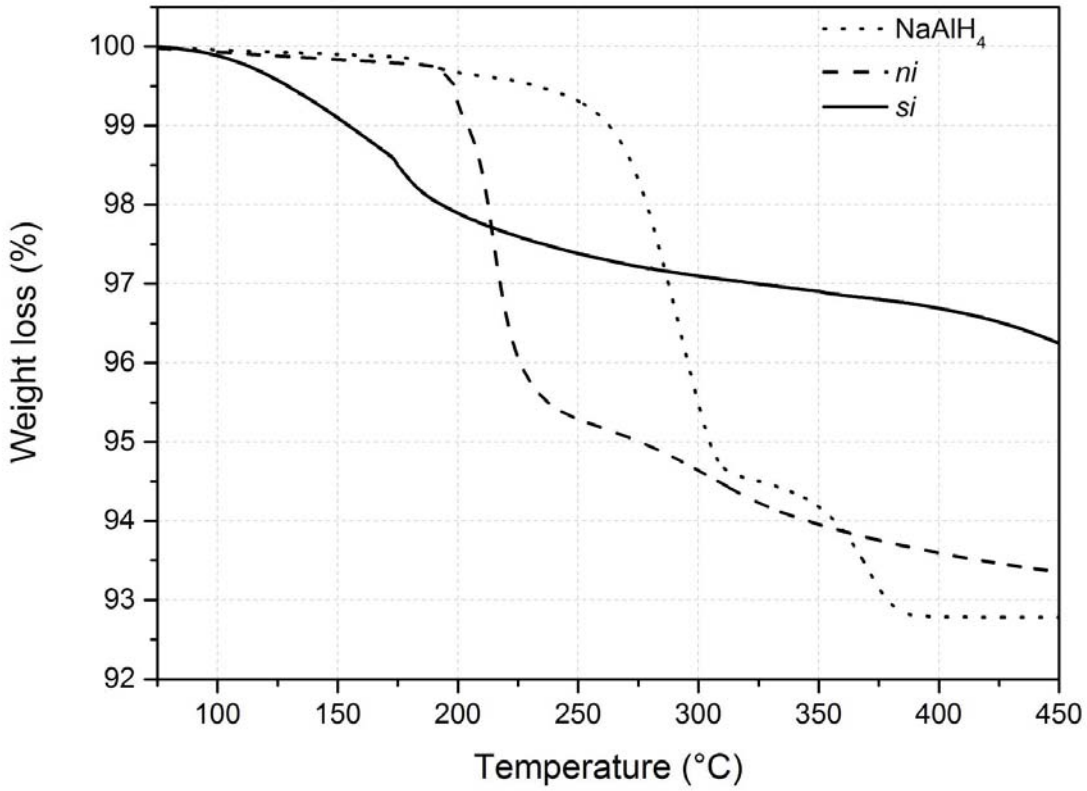
NaAlH4
ni
si
Weight loss (%)
Temperature (°C)
100
99
98
97
96
95
94
93
92
100
150
200
250
300
350
400
450

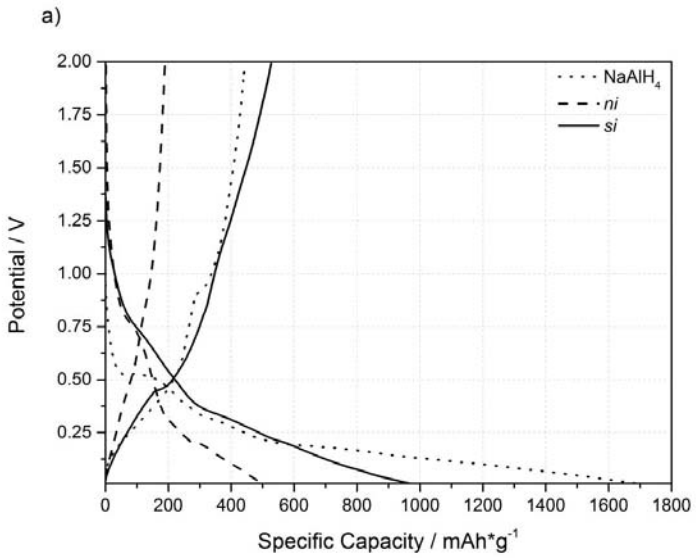
a)
Potential / V
Specific Capacity / mAh*g-1
NaAlH4
ni
si
2.00
1.75
1.50
1.25
1.00
0.75
0.50
0.25
0
200
400
600
800
1000
1200
1400
1600
1800

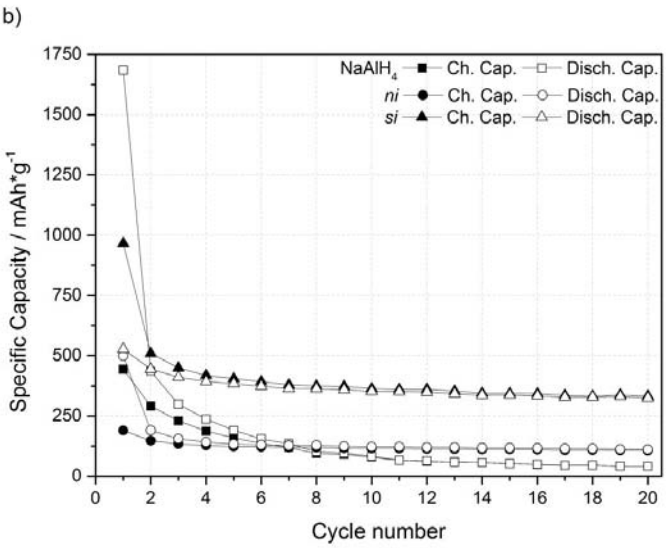
b)
Specific Capacity / mAh*g-1
Cycle number
NaAlH4 Ch. Cap. Disch. Cap.
ni Ch. Cap. Disch. Cap.
si Ch. Cap. Disch. Cap.
1750
1500
1250
1000
750
500
250
0
0
2
4
6
8
10
12
14
16
18
20